Examining Structural Inhomogeneities of Detonations in a Rotating Detonation Rocket Engine

Matthew Bonanni[a], Davy Brouzet[a], Guillaume Vignat[a], and Matthias Ihme[a,b]

[a]Department of Mechanical Engineering, Stanford University
440 Escondido Mall, Stanford, California, United States of America

[b]Department of Photon Science, SLAC National Accelerator Laboratory
2575 Sand Hill Rd, Menlo Park, California, United States of America

1 Introduction

Pressure-gain combustion is an alternative chemical propulsion technology with the potential to significantly improve the thermodynamic efficiency of aerospace propulsion systems [1, 2]. One implementation of a system using this technology is the rotating detonation rocket engine (RDRE). In contrast with other pressure-gain combustion devices, this system offers a continuous thrust output and has no moving parts. Typical RDRE designs comprise an annular combustion chamber with propellants injected at the head plane. One or multiple detonation waves propagate azimuthally around the chamber as fresh propellants are continuously injected. This design offers theoretically higher thermodynamic efficiency and power density [3] compared to deflagration-based devices. Furthermore, the viability of RDREs has been demonstrated in both laboratory [4] and space flight [5] settings.

RDRE injectors are typically non-premixed in practical designs, in order to prevent flashback. The short residence time between injection and combustion, however, leads to incomplete mixing of the propellants in the chamber [6]. This creates a significantly inhomogeneous mixture of fuel and oxidizer, which additionally includes combustion products left over from the prior detonation wave. This inhomogeneity can result in enlarged reaction zones, parasitic deflagrations, and commensal combustion [6, 7]. Regions of vitiated gases upstream of the detonation have also been shown to lead to a lower pressure ratio across the detonation wave [8, 9].

The present work presents a large-eddy simulation of an RDRE with a non-premixed injection system. In this simulation, Lagrangian tracer particles are used to track Eulerian state data along pathlines. This method enables analysis of detonation characteristics such as pressure ratio and velocity, and correlates these with local thermochemical conditions directly upstream of the detonation. Furthermore, this method enables analysis of spatial inhomogeneities of the detonation front, elucidating the relationship between mixing deficiencies and the resulting detonation properties.

2   Configuration

This work presents simulations of an experimental RDRE rig at AFRL [10], matching the conditions of the experiments by Bennewitz et al. [4, 11]. The injection system comprises 72 pairs of impinging jets through which oxygen and methane are fed, each from a common manifold. At the experimental conditions simulated here, the equivalence ratio is $\varphi = 1.16$ with a total mass flow rate of $\dot{m}_{tot} = 352\,\mathrm{g\,s^{-1}}$. While neither injector stream is choked, their high velocity stiffens them sufficiently in order to avoid flow reversal due to the passage of detonations [6]. The inlet boundary conditions for each manifold are located on their lower wall and the inlet temperature is set to $300\,\mathrm{K}$. At the combustor exit, flow is exhausted past a $15°$ aerospike nozzle into the atmosphere. In the simulation, this is represented by a cylindrical exhaust plenum with an axial co-flow of nitrogen.

3   Methods

In the present work, the geometry is discretized into an unstructured hybrid computational grid with a total of 54 million control volumes, as in Vignat et al. [12]. This mesh uses typical element sizes of $50\,\mathrm{\mu m}$ to $100\,\mathrm{\mu m}$, which is comparable to or finer than other meshes reported in the literature for this case and has been validated for this configuration [12].

The large-eddy simulation is performed using a fully compressible finite volume solver that solves the Favre-filtered continuity, momentum, energy, and species equations [13]. This solver has been previously validated for simulations of planar detonations [7].

For the spatial discretization, a high-order reconstruction retains fourth-order accuracy on uniform hexahedral meshes and third-order accuracy on non-uniform meshes [13]. Two shock sensors are used. The first, based on pressure and density gradients, is used to avoid numerical instabilities in the detonation, shock and combustion regions. The second is based on species mass fraction and temperature to avoid overshoots/undershoots of these scalars. A first order reconstruction procedure is then applied on the cells where the sensors are active.

Turbulent subgrid stresses (SGS) are represented using the Vreman model while constant turbulent Prandtl and Schmidt numbers of 0.7 are assumed for the turbulent SGS contribution to the heat flux and species diffusion.

A multi-species finite-rate chemistry approach is used with the 12 species, 38 reactions FFCMy-12 mechanism, specifically designed for high pressure methane-oxygen rocket engine combustion [14]. A simpler-balancing splitting scheme [15] for the advection-diffusion-reaction equations is used, where the stiff reaction time-stepping is treated with a fourth-order semi-implicit Rosenbrock-Krylov scheme while the non-stiff advection/diffusion operators are solved using a third-order strong stability preserving Runge-Kutta scheme. This increases the convective time step to a typical value of $4.3\,\mathrm{ns}$.

All walls in the domain are treated as no-slip and adiabatic. To ensure non-reflective acoustic behavior for the relevant frequencies, the locally one-dimensional and inviscid (LODI) Navier-Stokes characteristic boundary conditions (NSCBC) method is used to prescribe the inlet and outlet boundary conditions [16]. The relaxation coefficients have been tuned to achieve the desired behavior [7, 12]. To avoid inhomogeneities which could lead to spurious behavior at the outlet boundary condition, a sponge region is used in the exhaust plenum, with a linear relaxation factor in the streamwise direction for gradual application [17].

3.1 Lagrangian Particles

To analyze the characteristics of the detonations in the chamber, Lagrangian particles are used as passive tracers in the simulation. The particles are advanced in parallel with the Eulerian field using a second-order implicit (Crank-Nicolson) method, taking the local interpolated gas-phase velocity to be the instantaneous particle velocity. The particles are one-way coupled such that they have no effect on the flow field and do not interact with each other, and they track the local interpolated Eulerian state data for use in the detonation analysis.

Particles are injected at the base of the combustion chamber at a rate of approximately 10^9 particles per s, in order to effectively sample the cross section of the combustor at the full spatial resolution of the grid. At steady state, results and statistics were collected over a duration of $0.75\,\mathrm{ms}$, encompassing nine revolutions of each of the two detonation waves present in the chamber.

The data from the Lagrangian particles represent a time series of state variables over the particles' lifetimes in the chamber. From this data, ignoring particles which have passed an axial station of $y = 25\mathrm{mm}$, we may interpret each particle's spatiotemporal position at the moment of its detonation wave crossings. This information is inferred from each particle's pressure trace. The detonation crossings are localized as points of significant pressure gradient, and the peak pressure is recorded as the von Neumann state, p_2. Then, the state upstream along the particle's pathline is extracted as the pre-detonation state.

4 Results

An instantaneous sample of the solution from the simulation is presented in Fig. 1. As described in [12], the LES achieves agreement with experiments to within 3.2% of total thrust and 6.7% of specific impulse. In Fig. 1a, two detonation waves are visible in the chamber, moving in the $-\theta$ direction. They are co-rotating, with no counter-rotating waves. Typical post-detonation pressures reach $10\,\mathrm{bar}$. It is also evident that the detonations are not planar, with the downstream portion of the fronts leading the portion near the injection plane. We additionally note the regions of low temperature corresponding to the fresh reactants, reaching a filling height of approximately 25 mm before each detonation wave passage.

The section views in Figs. 1b to 1d demonstrate the inhomogeneity of the mixture ahead of the detonations due to the non-premixed injection. In Fig. 1b, we note the region of low temperature corresponding to the fresh reactants being injected into the chamber at 300 K. The jets impinge to promote mixing, but in Fig. 1d, depicting the mixture fraction, we note the strongly rich and lean sides of the chamber corresponding to the fuel and oxygen injectors, respectively. The inhomogeneity reduces with axial distance, as the propellant jets mix. Additionally, it is evident from Figs. 1b and 1c that there is a significant presence of hot combustion products still present in the lower parts of the chamber, especially on the outside of the chamber near the oxygen injector. A small pocket of products is present on the fuel side as well.

Using the data extracted via the method described in Section 3, we can conditionally average over radial and axial position to reconstruct the inhomogeneities of the pre-detonation state, as depicted in Fig. 2. We can then determine the shape of the detonations by grouping the data into temporal bins, computing an average azimuthal position, and calculating the azimuthal offset of each intersection. This result is then conditionally averaged over time to determine the mean detonation shape, as depicted in Fig. 2e.

Firstly, in Fig. 2a, we note that the strength of the detonation is not uniform across the cavity. There is a pocket of high-strength detonations on the interior side where the fuel is injected, at an axial station
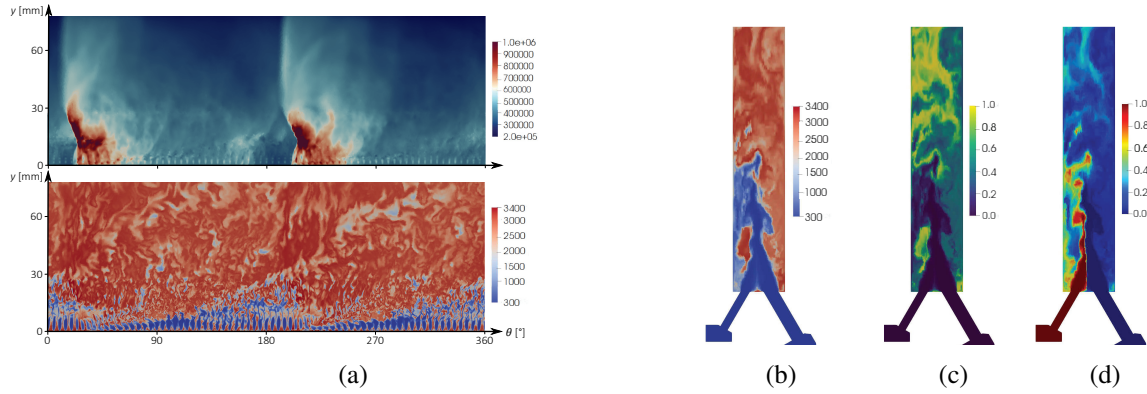
(a)

Figure 1: Instantaneous LES solutions. (a) pressure (top, Pa) and temperature (bottom, K) fields of the combustion chamber, unwrapped view at the chamber mid-cylinder ($r = 35.6$ mm). (b) temperature (K), (c) progress variable, and (d) mixture fraction are section views showing the lower 25 mm of the chamber and the two injection ports. A detonation front is approximately two injectors downstream from the location of this section. Reproduced from Vignat et al. [12].
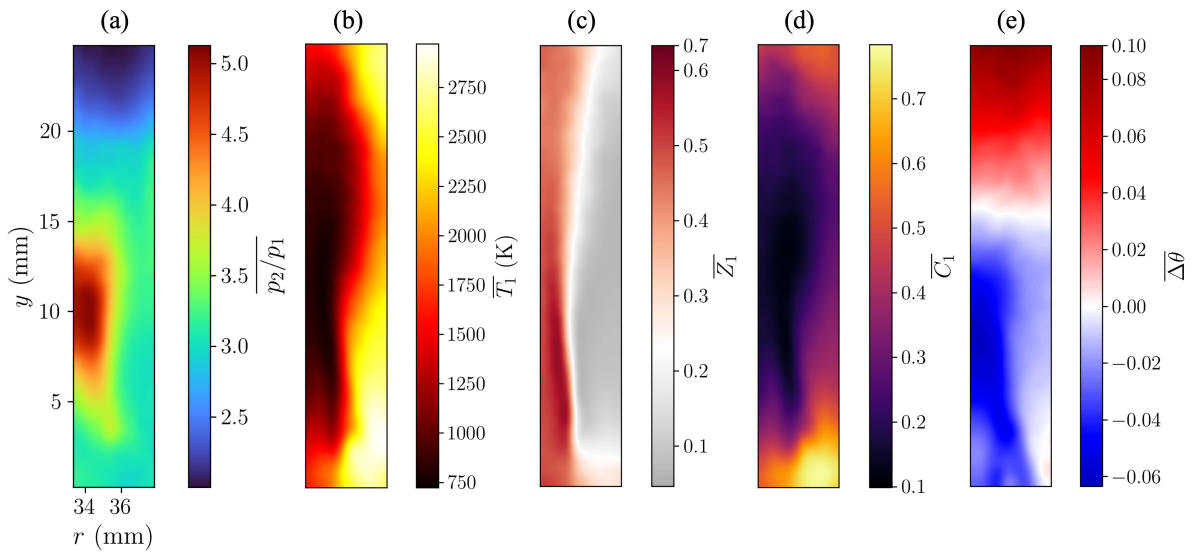

Figure 2: Temporally averaged detonation properties, conditioned on radial and axial position in combustion chamber. (a) pressure ratio across detonation, (b), pre-detonation temperature K, (c), pre-detonation mixture fraction, with colormap centered at $Z_{gl} = 0.23$, (d), pre-detonation progress variable, and (e), detonation deformation.

of 10 mm. At this position, the pressure ratio across the detonation reaches values greater than 5. The strength of the detonation higher in the chamber reduces to a value of 2 as the filling height is approached. Figure 2b and Fig. 2d agree with observations from the instantaneous field in Fig. 1b that there is significant presence of hot combustion products in the lower chamber on the side of the oxygen injector. The mixing deficiency is particularly highlighted in Fig. 2c, where there is a distinct separation of rich and lean sides in the cavity. This inhomogeneity appears to be correlated with the strength of the detonation in Fig. 2a, with the strongest region of the detonation occurring on the rich side of the cavity. Finally, we observe the significant deformation of the detonation front in Fig. 2e. In the upper part of the chamber, the front significantly leads the average, whereas there is a pocket at station $y = 10$mm which

significantly lags. Interestingly, this appears to be highly correlated with the strength of the detonation, with the weakest detonations leading the front and the strongest detonations lagging.

We can elucidate these correlations by building conditional probability distribution functions of the particle-front intersection data, as depicted in Fig. 3. In Fig. 3a, we note that the strongest detonations occur at low and high mixture fractions, and the detonations weaken near the stoichiometric mixture fraction. The relationship with pre-detonation progress variable is shown in Fig. 3b, where it is evident that vitiation of the upstream gases reduces the pressure ratio across the detonation, a result that agrees with prior work [8]. Finally, we note the relationship between detonation strength and deformation in Fig. 3c, demonstrating that the pressure ratios are typically low when the front leads upstream, and high when the detonation lags, with the exception of the most extreme lagging cases, though the data here becomes increasingly sparse.
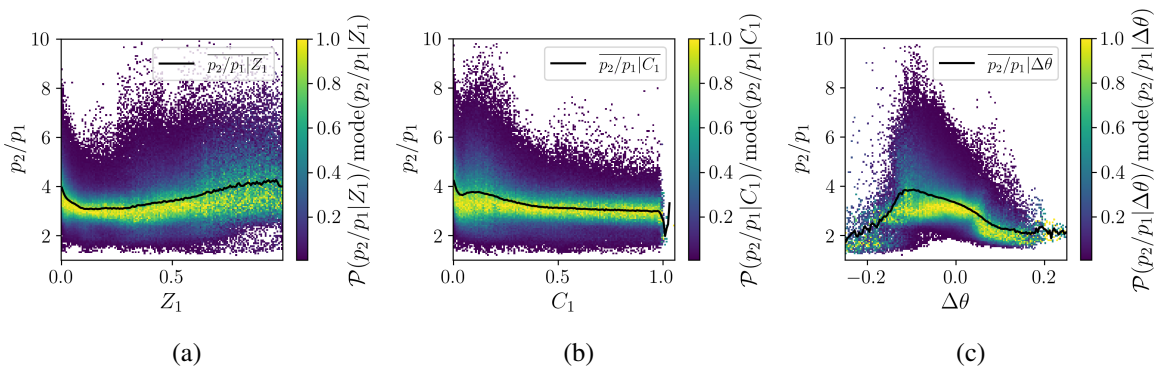

Figure 3: Probability distribution functions of detonation strength conditioned on (a), pre-detonation mixture fraction, (c), pre-detonation progress variable, and (c), detonation deformation.

5 Conclusions

This study presented a high-fidelity three-dimensional large-eddy simulation of an RDRE, obtaining a solution with two waves which agrees with experiments in engineering quantities of interest such as thrust, chamber pressure, and specific impulse. The unique analytical access that such a simulation provides was then exercised to perform a study of spatial inhomogeneities in the detonation topology. A Lagrangian technique was applied, in which pre- and post-detonation states were extracted along particle trajectories. The resulting data demonstrated the presence of significant mixing deficiencies in the combustor, as well as significant vitiation of the reactants ahead of the detonation via mixing with combustion products and deflagration. The pressure ratio across the detonation is significantly impacted by these effects, with the highest pressure ratios occurring at very lean or very rich conditions with low vitiation. Finally, the shape of the detonation front is correlated with the pressure ratio across the detonation - regions with low pressure ratios tend to lead the front, whereas regions with high pressure ratios tend to lag.

Acknowledgements

References

[1] F. K. Lu, E. M. Braun, J. Powers, Rotating detonation wave propulsion: Experimental challenges, modeling, and engine concepts, Journal of Propulsion and Power 30 (2014) 1125–1142.

[2] P. Wolański, Detonative propulsion, Proc. Combust. Inst. 34 (2013) 125–158.

[3] R. Yokoo, K. Goto, J. Kim, A. Kawasaki, K. Matsuoka, J. Kasahara, A. Matsuo, I. Funaki, Propulsion performance of cylindrical rotating detonation engine, AIAA Journal 58 (2020) 5107–5116.

[4] J. W. Bennewitz, B. R. Bigler, W. A. Hargus, S. A. Danczyk, R. D. Smith, in: AIAA Joint Propulsion Conference, pp. 1–22.

[5] K. Goto, K. Matsuoka, K. Matsuyama, A. Kawasaki, H. Watanabe, N. Itouyama, K. Ishihara, V. Buyakofu, T. Noda, J. Kasahara, A. Matsuo, I. Funaki, D. Nakata, M. Uchiumi, H. Habu, S. Takeuchi, S. Arakawa, J. Masuda, K. Maehara, T. Nakao, K. Yamada, in: AIAA SciTech Forum.

[6] S. Prakash, V. Raman, C. F. Lietz, W. A. Hargus, S. A. Schumaker, Numerical simulation of a methane-oxygen rotating detonation rocket engine, Proc. Combust. Inst. 38 (2021) 3777–3786.

[7] D. Brouzet, G. Vignat, M. Ihme, Dynamics and structure of detonations in stratified product-gas diluted mixtures, Proc. Combust. Inst. (2022).

[8] F. Chacon, M. Gamba, in: AIAA Scitech 2019 Forum, January.

[9] J. Fujii, Y. Kumazawa, A. Matsuo, S. Nakagami, K. Matsuoka, J. Kasahara, Numerical investigation on detonation velocity in rotating detonation engine chamber, Proc. Combust. Inst. 36 (2017) 2665–2672.

[10] R. D. Smith, S. B. Stanley, Experimental Investigation of Rotating Detonation Rocket Engines for Space Propulsion, Journal of Propulsion and Power 37 (2021) 463–473.

[11] C. F. Lietz, Y. Desai, o. Hargus, V. Sankaran, in: AIAA Propulsion and Energy Forum and Exposition, 2019.

[12] G. Vignat, D. Brouzet, M. Bonanni, M. Ihme, Effect of secondary waves on mixing and injector near-field dynamics in non-premixed rotating detonation engine, Shock Waves (2023, (under review)).

[13] P. C. Ma, Y. Lv, M. Ihme, An entropy-stable hybrid scheme for simulations of transcritical real-fluid flows, Journal of Computational Physics 340 (2017) 330–357.

[14] R. Xu, K. Wang, S. Banerjee, J. Shao, T. Parise, Y. Zhu, S. Wang, A. Movaghar, D. J. Lee, R. Zhao, X. Han, Y. Gao, T. Lu, K. Brezinsky, F. N. Egolfopoulos, D. F. Davidson, R. K. Hanson, C. T. Bowman, H. Wang, A physics-based approach to modeling real-fuel combustion chemistry – II. Reaction kinetic models of jet and rocket fuels, Combustion and Flame 193 (2018) 520–537.

[15] H. Wu, P. C. Ma, M. Ihme, Efficient time-stepping techniques for simulating turbulent reactive flows with stiff chemistry, Computer Physics Communications 243 (2019) 81–96.

[16] T. Poinsot, S. K. Lele, Boundary conditions for direct simulations of compressible viscous flows, Journal of Computational Physics 101 (1992) 104–129.

[17] C. Bogey, C. Bailly, D. Juve, Numerical simulation of sound generated by vortex pairing in a mixing layer, AIAA Journal 38 (2000) 2210–2218.